Elsevier Editorial System(tm) for Materials Science and Engineering C

Manuscript Draft

Manuscript Number:

Title: SYNTHESIS AND CHARACTERIZATION OF STRONTIUM-SUBSTITUTED HYDROXYAPATITE NANOPARTICLES FOR BONE REGENERATION

Article Type: Research Paper

Corresponding Author: Mr. Matteo Frasnelli,

Corresponding Author's Institution: DII - University of Trento

First Author: Matteo Frasnelli

Order of Authors: Matteo Frasnelli; Francesco Cristofaro; Vincenzo M Sglavo; Sandra Dirè; Emanuela Callone; Riccardo Ceccato; Giovanna Bruni; Antonia I Cornaglia; Livia Visai

Abstract: The production of stable suspensions of strontium-substituted hydroxyapatite nanopowders as Sr ions vector for bone tissue regeneration was studied in the present work. Sr-HA nanopowders were synthesized via aqueous precipitation methods using Sr2+ amount from 0% to 100% and were deeply characterized by several complementary techniques such as solid-state NMR spectroscopy, X-ray diffraction, FT-IR spectroscopy, N2 physisorption, and TEM. The substitution of Ca2+ with Sr2+ in HA was responsible for a significant variation of the nanopowders dimension, with increasing preferential growth along the direction parallel to c-axis, and caused modifications in the local chemical environment of phosphate and hydroxyl groups in the apatite lattice.
The suspensions were produced by dispersing the synthesized nanopowders in bovine serum albumin (BSA) and were characterized by Dynamic Light Scattering (DLS) and ζ-potential determination. The biocompatibility of the suspensions was studied in terms of cell viability, apoptosis, proliferation and morphology, using SAOS-2 cells. The data pointed out an increased cell proliferation for HA nanoparticles containing larger Sr2+ load, the cells morphology remaining essentially unaffected.

Cover letter

In this work, strontium-substituted hydroxyapatite (Sr-HA) nanoparticle suspensions were produced using bovine serum albumin as dispersant agent as an innovative potential tool to improve bone tissue regeneration. The choice of such specific inorganic materials is to be found in the biological affinity between synthetic HA and the inorganic portion of human bone, as well as in the well-known osteoinductive property of strontium.

Testing the suspensions with osteoblasts-like cells, Sr-HA nanoparticles were shown to be perfectly biocompatible and are able to improve osteoblast proliferation.

The performed work supplies a complete overview on the influence of substitutional strontium within the hydroxyapatite structure over different hierarchical levels (nanopowder morphology, crystalline structure, functional groups and corresponding chemical environment) providing a starting point for the comprehension of its interaction with biological systems.

Suggested Reviewers

- Joanna Kolmas, joanna.kolmas@wum.edu.pl
- Ennio Tasciotti, etasciotti@houstonmethodist.org
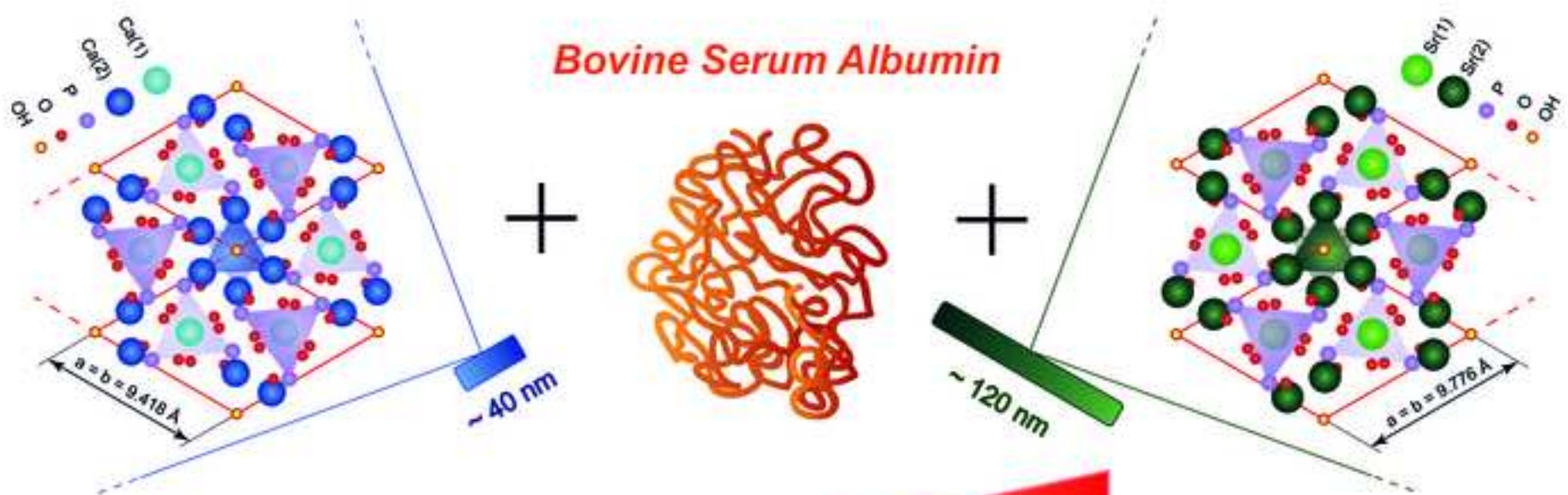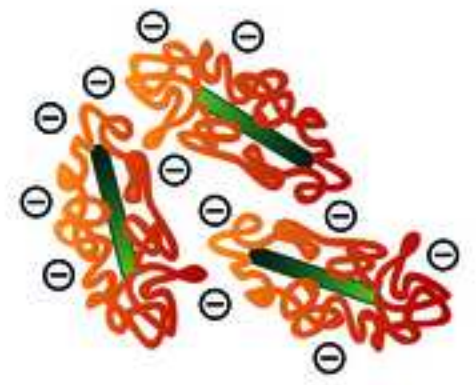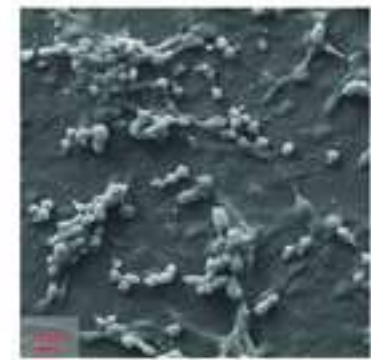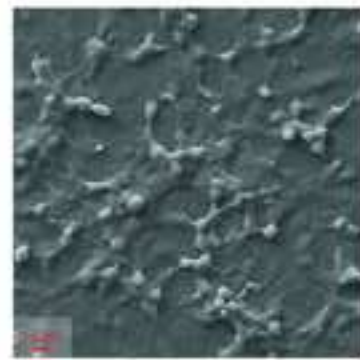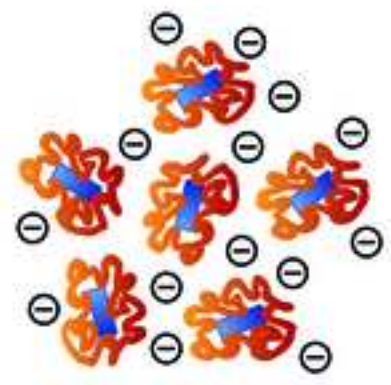
Graphical Abstract

SYNTHESIS AND CHARACTERIZATION OF STRONTIUM-SUBSTITUTED HYDROXYAPATITE NANOPARTICLES FOR BONE REGENERATION

Matteo Frasnelli[1,6*], Francesco Cristofaro[2*], Vincenzo M. Sglavo[1,6], Sandra Dirè[1,7], Emanuela Callone[1,7], Riccardo Ceccato[1], Giovanna Bruni[3], Antonia Icaro Cornaglia[4], Livia Visai[2,5]

[1]Department of Industrial Engineering, University of Trento, Via Sommarive 9, 38123 Trento, Italy. Tel +39 0461 281977

[2]Department of Molecular Medicine, Center for Health Technologies (CHT), University of Pavia, Viale Taramelli 3/b, 27100 Pavia, Italy. Tel +39 0382 987179

[3]Department of Chemistry, Physical-Chemistry Section, University of Pavia, Viale Taramelli 16, 27100, Pavia (PV), Italy

[4]Department of Experimental Medicine, Faculty of Medicine, University of Pavia, Italy

[5]Department of Occupational Medicine, Toxicology and Environmental Risks, S. Maugeri Foundation, IRCCS, Via S. Boezio, 28, 27100, Pavia (PV), Italy

[6]INSTM Research Unit, Via G. Giusti 9, 50123 Firenze, Italy

[7]"Klaus Müller" NMR Laboratory, Department of Industrial Engineering, University of Trento, Via Sommarive 9, 38123 Trento, Italy

*Both authors contributed equally to this article.

Corresponding author:

Matteo Frasnelli

matteo.frasnelli@unitn.it

Department of Industrial Engineering, University of Trento, Via Sommarive 9, 38123 Trento, Italy. Tel +39 0461 281977

VITAE

Matteo Frasnelli received his master of Materials Engineering from the University of Trento, Italy, where he is currently undertaking his PhD program in Materials, Mechatronics and Systems Engineering. His research interests include synthesis of calcium phosphate bioceramics, their characterization by thermal and spectroscopy techniques and their consolidation by conventional and electrical field-assisted sintering processes.

Francesco Cristofaro is a Ph.D. student at the University of Pavia in Biomedical Science at Molecular Medicine Department. His project is about Nanoparticles engineered to improve bone formation modulating osteoblast and osteoclast activities. He worked with European and Italian space agencies to test nanoparticles' effect in microgravity condition. During his master thesis project at the University of Brighton, Cristofaro has developed knowledge and expertise about synthesis, characterization and biocompatibility evaluations of several types of nanoparticles. Nowadays he takes part in further projects about interaction between materials and cells to develop new biomaterial for tissue engineering applications.

Dr. Giovanna Bruni is Researcher at the School of Pharmacy of the University of Pavia. The long experience in the field of the physic-chemical characterization of pharmaceutical solids and the expertise gained in the use of thermal techniques and electron microscopy are the basis for an activity of problem solving in the pharmaceutical industry, for example in relation to the phenomena of polymorphism, pseudo-polymorphism and amorphism, the drug-excipient compatibility and the investigation of strategies to improve the solubility and other properties of drugs. The research activity is documented by about ninety scientific publications on peer-reviewed international journals.

Antonia Icaro Cornaglia - born in Pavia, on 4 June 1962 - graduated cum laude in Biology in 1987, is Researcher of Histology since 1998 at the University of Pavia, Department of Public Health, Neuroscience, Experimental and Forensic Medicine, Histology Unit. She is member of

the Italian Society of Anatomy and Embryology and is involved in several research projects, both at the local and national levels. Main scientific interests include cell proliferation and differentiation both in human tissues and in experimental models. In the last years her interest is oriented on stem cells and tissue and organ engineering, particularly on engineered skin and skeletal tissues (cartilage and bone).

Dr. Livia Visai is an Associate Professor in Biochemistry at the Medicine Faculty of Pavia University (Italy). She received her degree in Biological Science in 1985 and the Ph.D in Biochemistry in 1989, both titles at Pavia University. She had been working at the University of Alabama in Birmingham (USA), at the Center for Infectious and Inflammatory Diseases, Texas A&M University of Houston (USA). She has been Vice-Director of the Interdepartmental Center for Tissue Engineering and now she is the referent of the academic strategic project, Center for Health Technologies (CHT) in Pavia. In 2011, she received an apical position at the Salvatore Maugeri Foundation, Pavia.

ABSTRACT

The production of stable suspensions of strontium-substituted hydroxyapatite nanopowders as Sr ions vector for bone tissue regeneration was studied in the present work. Sr-HA nanopowders were synthesized via aqueous precipitation methods using Sr^{2+} amount from 0% to 100% and were deeply characterized by several complementary techniques such as solid-state NMR spectroscopy, X-ray diffraction, FT-IR spectroscopy, N_2 physisorption, and TEM. The substitution of Ca^{2+} with Sr^{2+} in HA was responsible for a significant variation of the nanopowders dimension, with increasing preferential growth along the direction parallel to c-axis, and caused modifications in the local chemical environment of phosphate and hydroxyl groups in the apatite lattice.

The suspensions were produced by dispersing the synthesized nanopowders in bovine serum albumin (BSA) and were characterized by Dynamic Light Scattering (DLS) and ζ-potential determination. The biocompatibility of the suspensions was studied in terms of cell viability, apoptosis, proliferation and morphology, using SAOS-2 cells. The data pointed out an increased cell proliferation for HA nanoparticles containing larger Sr^{2+} load, the cells morphology remaining essentially unaffected.

1. INTRODUCTION

Calcium phosphate ceramics, *e.g.* hydroxyapatite $Ca_{10}(PO_4)_6(OH)_2$ (HA) and tricalcium phosphate $Ca_3(PO_4)_2$ (TCP), are widely employed in the field of bone tissue engineering due to their controlled biodegradability and excellent biocompatibility[1–4]. Pure HA possesses a bi-pyramidal hexagonal crystal structure (space group $P6_3/m$, a = b = 9.418 Å, c = 6.884 Å, $\alpha = \beta = 90°$, $\gamma = 120°$) where PO_4^{3-} tetrahedrons are regularly placed on two basal planes at ¼ and ¾ of the c-axis. Considering an unit cell, ten Ca^{2+} ions are located within two non-equivalent interstitial sites, four M(1) sites aligned to the c-axis at the cell edges and six M(2) sites forming two staggered equilateral triangles, placed above the phosphate basal plane. Within this triangular channel along the *c-axis* the two OH^- groups are placed.

The mineralized phase of bones, as well as enamel and dentin, is associated to nano-sized crystallites of calcium deficient HA [5], partially enriched by a large variety of substitutional ions. For example, one of the most common isomorphic ion replacement consists in the carbonatation of HA through the substitution of PO_4^{3-} or OH^- by CO_3^{2-} groups,

up to ~7%w [6]. In addition, biological apatites can also rearrange the presence of Mg^{2+}, Sr^{2+}, F^-, Cl^- or HPO_4^{2-} [7–10] within their crystal structure, influencing the biological behaviour of the material. In particular, strontium is strictly related to the bone response to osteoporosis, by promoting new tissue growth and decreasing its resorption.

The interest in the role of strontium in bone biology dates back to the end of the XIX century. Most studies point out that the incorporation of Sr in the bone occurs quite rapidly (within the first two weeks) [11]; X-ray diffraction analyses (XRD) show the distortions of the bone mineral crystals unit cell caused by Sr, confirming the incorporation of such alkaline ion into the crystalline lattice. Since then, after the development of the promising drug strontium ranelate (SR), different types of studies were performed from mapping Sr in bones and teeth, to studying the incorporation of Sr into bone mineral (in particular in the crystal surface and lattice) and the decrease in calcium content, up to evaluate the effects of Sr in synthetic HA [12]. SR is currently used in the treatment of post-menopausal osteoporosis [13], although its prescription has been recently restricted to the acute medical cases because of cardiovascular side effects [14]. SR shows a dual beneficial action, enhancing the pre-osteoblastic cells differentiation and inhibiting the osteoclastic cells formation and functionality.

In a previous work [15], strontium has been shown to completely replace calcium ions in both non-equivalent interstitial sites. Due to the ionic radius difference (Ca^{2+} = 0.100 nm, Sr^{2+} = 0.118 nm), the presence of strontium results in a general perturbation of the lattice, increasing the cell parameters and the mean size of the crystal domains. In addition, previous *in vitro* and *in vivo* studies of the biological reactivity of Sr-substituted HA embedded in scaffolds like coatings on titanium components [16, 17], gels [18], membranes [19] or tablets [20] in terms of cell vitality, proliferation and morphology have shown the osteogenic effect of Sr-HA. If these studies are relevant because they present potential effects that the incorporation of Sr could have on bone mineral, so far no studies were performed to develop and characterize stable suspension of strontium-substituted HA nanoparticles as a vector for Sr ions delivery for bone tissue engineering applications. For *in vitro* biocompatibility studies, a suitable agent must be selected to produce stable aqueous suspensions, avoiding nanoparticles flocculation [21, 22] and growth by Ostwald ripening-like process. In addition, the dispersant should not have any effect on the test system, such as cell lines, microorganisms and animals. Bovine Serum Albumin (BSA) is a biological and mimic fluid and in a previous study was used as dispersant agent to obtain stable nanoparticles suspension [23], preventing toxic effects due to powder agglomeration. Therefore, in this work, BSA has been used for preparing nanoparticles suspension for biocompatibility evaluation.

The aim of the present work was to synthesize Sr-doped HA nanopowders and to investigate the effect of Sr presence within the apatite lattice by an extensive chemical, structural and morphological characterization of the powders. The synthesized Sr-doped HA nanopowders were then used to produce stable suspensions, analyse their efficiency on osteoblast viability and understand their suitability as nano-carriers for Sr delivery in the stimulation of bone tissue regeneration.

2. MATERIALS AND METHODS

2.1 HA nanopowders: synthesis and suspensions preparation

HA nanopowders containing various Sr^{2+} amount were synthesized by aqueous precipitation method, as reported in a previous work by Bigi et al. [15]. High-purity calcium nitrate tetrahydrate ($Ca(NO_3)_2 \cdot 4H_2O$, 99%w, Sigma Aldrich A.C.S. reagent), strontium nitrate anhydrous ($Sr(NO_3)_2$, 98%w, Alfa Aesar) and ammonium phosphate dibasic (($NH_4)_2HPO_4$, >99.0%w, Fluka), were respectively used to prepare the Ca+Sr nitrate solutions (50 mL, 1.08 M overall) and the phosphate solutions (50 ml, 0.65 M), adjusted at pH 10 with NH_4OH (30%v). The synthesis was carried out in N_2 constant flow, to avoid as much as possible the carbonatation phenomena, adding drop-wise the phosphate solution to the nitrate solution at 90°C under stirring. The solution was stirred at 90°C in N_2 static atmosphere for 5 h; then, the white precipitate was centrifuged three times (10000 rpm for 10 min), washed and finally dried at 80°C overnight. The strontium content in the final HA powder was tailored changing the relative amount of $Ca(NO_3)_2 \cdot 4H_2O$ and $Sr(NO_3)_2$ in the nitrate solutions, to obtain a Sr/(Sr+Ca) molar ratio of 0, 5, 10, 25, 50, 75 and 100%; pure HA and Sr-doped HA nanopowders were labelled as Ca100 and SrX (X = molar amount of Sr), respectively.

To obtain a stable suspension, 5 mg of powder were added to 4 mL of 5% BSA (Sigma-Aldrich) aqueous solution. The suspension was sonicated for 1 h at 45°C using LBS2 sonicator bath (FALC Instruments) with an operation frequency of 40 kHz and then diluted with Phosphate Buffer Solution (PBS). The obtained suspensions were labelled adding the suffix "S" to the powder label (*e.g.*, SrXS).

2.2 Characterization techniques and procedures

2.2.1 Inductively coupled plasma optical emission spectrometry (ICP-OES): The synthesized powders purity and composition were determined by ICP-OES (Spectro Ciros Vision CCD, 125-770 nm) using hydroxyapatite ultrapure standard (Reagent Grade, Sigma-Aldrich) and a 1000 ppm Sr standard (BHD SpectroSol). All samples and standards were

dissolved in ultrapure nitric acid (70%v) and diluted in pure water from reverse osmosis (conductivity < 0.1 μS/cm), adding Cs (100 g/L) as ionization suppressor. The emission lines chosen for the analysis were 393.366 nm for Ca, 216.596 nm for Sr and 178.287 nm for P.

2.2.2 Fourier transform infrared spectroscopy (FTIR): FTIR spectra were acquired in transmission mode using an Avatar Thermo FTIR spectrometer on KBr pellets in the range of 4000-400 cm^{-1} (resolution = 4 cm^{-1}, 64 scans). With the aim to investigate the interaction between nanopowders and bovine serum albumin (BSA), ATR-FTIR spectra were recorded on the suspensions previously lyophilized. Physical mixtures were also prepared merely blending 5 mg of each synthesized nanopowder with 200 mg of BSA to be compared with the data collected on the suspensions. ATR-FTIR spectra were recorded in the 4000–650 cm^{-1} range (resolution = 4 cm^{-1}, 256 scans) using a Nicolet FT-IR iS10 Spectrometer (Nicolet, Madison, WI, USA) equipped with a ZnSe plate ATR (Attenuated Total Reflectance) sampling accessory.

2.2.3 Nitrogen sorption: N_2 physisorption analyses were carried out on a Micromeritics ASAP 2010 analyser. Specific surface area (SSA) and volume pore distributions were calculated from N_2 adsorption/desorption isotherms applying BET equation and BJH model, respectively.

2.2.4 X-ray diffraction (XRD): The mineralogical composition of the synthesized Sr-HA powders was analysed by XRD using a Rigaku DMAX III 4057A2 diffractometer, working at 40 kV and 30 mA (Cu K_α: 1.5418978 Å). All data were collected in the range 2θ = 10°-60°, with step size of 0.03° and dwell time of 10 s/step. Spectra were analysed by the Rietveld-method-based software MAUD (2.53 version), using PDF cards #09-0432 - Calcium-hydroxyapatite and #33-1348 - Strontium-hydroxyapatite as structural models.

2.2.5 Solid state nuclear magnetic resonance (NMR): ^{31}P and ^1H solid state NMR analysis were carried out with a Bruker 300WB instrument. Samples were packed in 4 mm ZrO_2 rotors, which were spun by air flow at 11 kHz under MAS conditions. The ^{31}P SP-MAS experiments were recorded at the frequency of 121.49 MHz, with a single pulse sequence under the following conditions: $\pi/2$ pulse of 3.6 μs, recycle delay 300 s, 16 scans, using high-power proton decoupling during signal acquisition. The ^{31}P cross-polarization spectra (^{31}P CP-MAS) were recorded with a contact time of 0.5 ms, 100 scans. In both cases, ammonium dihydrogen phosphate $NH_4H_2PO_4$ was used as secondary reference. The ^1H MAS experiments were run at frequency of 300.13 MHz, $\pi/2$ pulse of 5 μs, recycle delay 5 s, 16 scans. Pure ethanol was used as secondary reference.

2.2.6 Transmission electron microscopy (TEM): In order to investigate the powder size and morphology, 5 mg of powder were dissolved in acetone and sonicated for 10 min; 10

µL of the suspension were deposited on a formvar coated copper grid (Electron Microscopy Sciences), allowing solvent evaporation overnight. Images of each sample were acquired by Zeiss EM 10 transmission electron microscope operating at 80 kV.

2.2.7 Dynamic light scattering (DLS): Hydrodynamic diameter and ζ potential of nanoparticle suspensions kept at 37°C for 1, 3, 7, 14 and 30 days were measured using dynamic light scattering (DLS) technique with Zetasizer Nano-ZS90 (Malvern Instruments).

2.3 Biocompatibility studies

2.3.1 Cell culture condition: The human osteosarcoma cell line SAOS-2 was acquired from the American Type Culture Collection (HTB85, ATCC, Manassas, VA, USA). The cells were cultured in McCoy's 5A modified medium (Lonza) with L-glutamine (Lonza) supplemented with 15% fetal bovine serum (EuroClone), 1% sodium pyruvate (Lonza), 1% antibiotics (Lonza) and 0.2% amphotericin B (Lonza). Cells were cultured at 37°C with 5% CO_2, routinely trypsinized after confluency, counted and seeded. The cells were treated with three concentrations (6.25 µg/mL, 62.5 µg/mL and 625 µg/mL) of each suspension in the culture medium. The cells were treated for 1, 3 and 7 days changing medium two times per week. Untreated cells were used as negative control.

2.3.2 Cell apoptosis: To determine the induction of cell apoptosis by the nanoparticle suspensions, SAOS-2 cells were labelled using the PSVue480™ cell stain according to the manufacturer's instructions (Molecular Targeting Technologies, Inc.). PSVue480™ dye detects apoptosis by targeting the loss of phospholipid asymmetry in the plasma membrane that is an early event in apoptosis, independent of cell type, resulting in the exposure of phosphatidylserine (PS) residues at the outer plasma membrane leaflet [24]. SAOS-2 cells were seeded on glass coverslips (Thermo Scientific) with a density of 5×10^4 cells/cm^2 and incubated with H_2O_2 (positive controls; 100 mM for 18 h), without suspensions (negative controls) and with 6.25 µg/mL, 62.5 µg/mL and 625 µg/mL of each suspension for 1 and 7 days. At the end of each culture condition, the cells were stained with PSVue480™ solution prepared according to manufacturer's instructions. Samples were then counterstained with a Hoechst 33342 solution (2 µg/mL) to target the cellular nuclei and observed under a fluorescence optical microscope (Nikon Eclipse 80i).

2.3.3 MTT test: Mitochondrial activity was evaluated using 3-(4,5-dimethylthiazole-2-yl)-2,5-diphenyl tetrazolium bromide (MTT) test (Sigma-Aldrich). The viability assay was carried out at day 1, 3 and 7 (end of the culture period) as previously reported [25]. Aliquots of 100 µL were sampled and their absorbance was measured at reference wavelengths of 595 nm and 650 nm by a microplate reader (BioRad Laboratories, Hercules, CA, USA).

2.3.4 Resazurin-based assay: The resazurin-based assay was used to estimate the number of viable cells by measuring the reduction of resazurin into resorufin. Resazurin solution (Sigma-Aldrich) was added as one-tenth of culture volume to each well of the plate, which was then incubated for 3 h at 37°C and 5% CO_2. Optical measurements were run on aliquots of 100 μL by a microplate reader (BioRad Laboratories, Hercules, CA, USA) at reference wavelengths of 600 nm and 690 nm at day 1, 3 and 7 (end of the culture period) on treated and untreated cells. A cell viability standard curve was used to express the results as number of alive cells.

2.3.5 Scanning electron microscopy (SEM): Treated and untreated cells morphology was investigated by scanning electron microscopy (SEM) after 1 and 7 days treatment; samples were fixed with 2.5%v glutaraldehyde solution in 0.1 M Na-cacodylate buffer (pH=7.2) for 1 h at 4°C, washed with Na-cacodylate buffer and then dehydrated at room temperature in a gradient ethanol series up to 100%. To obtain a complete dehydration, samples were lyophilized for 3 h. Samples were then sputtered with gold and observed using a Zeiss EVO-MA10 (Carl Zeiss, Oberkochen, Germany) SEM.

2.4 Statistical analysis

In all quantitative tests, cell treatments were performed in triplicate and the results of three independent experiments were considered. In order to compare the viability results between treated and untreated cells at day 1, 3 and 7, the one-way analysis of variance (ANOVA) with post hoc Bonferroni test was applied, with a significance level of 0.05.

3. RESULTS

3.1 Nanopowders and suspensions characterization

The chemical analysis of the synthesized nanopowders shows a slight Sr^{2+} deficiency compared with the nominal values, especially for the lowest Sr contents (Tab. 1). Conversely, the measured (Ca+Sr)/P ratio is in the range of 1.771 - 1.537 for Sr5 and Sr75, respectively, very close to the stoichiometric Ca/P ratio for pure HA, equal to 1.667.

Sample	Ca100	Sr5	Sr10	Sr25	Sr50	Sr75	Sr100
Sr^{2+} nominal content, mol%	0	5	10	25	50	75	100
Sr/(Ca+Sr), mol%	0.0	4.2	7.4	21.3	45.2	74.2	100.0
(Ca+Sr)/P, at. ratio	1.743	1.771	1.614	1.670	1.652	1.537	1.570

Tab. 1: Strontium content in the synthesized Sr-HA nanopowders and calculated metals-to-phosphorus atomic ratio (measured by ICP-OES).

Despite such limited compositional differences, FT-IR spectra of Sr-HA samples (Fig. 1) are in good agreement with the characteristic PO_4^{3-} and OH^- vibrations in the HA lattice reported in the literature [26]. The absence of the doublet at 1466 and 1411 cm^{-1}, associated to CO_3^{2-} groups [27], proves the efficiency of the reaction conditions used here; conversely, the presence of adsorbed water is shown by the very broad signals around 3440 cm^{-1} and 1630 cm^{-1}.
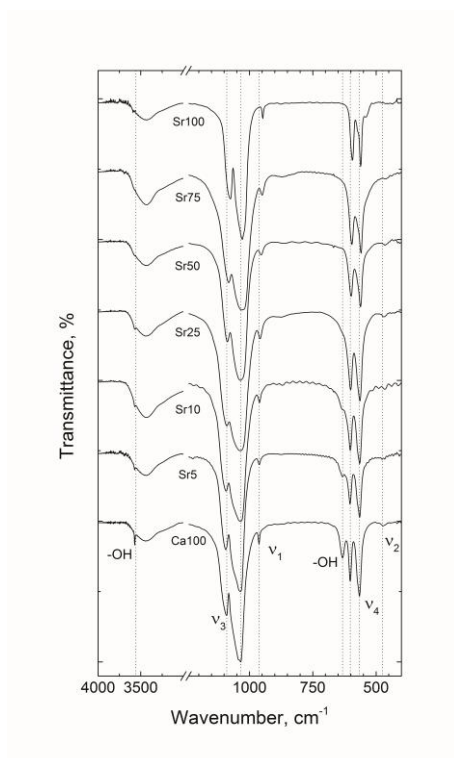

Fig 1: FT-IR spectra of the synthesized Sr-Hydroxyapatite nanopowder. Vertical dotted lines are referred to the frequencies of interest in the Ca100 spectrum.

From a qualitative point of view, the phosphate bands are affected by progressive signal shifts to lower wavenumbers with increasing Sr^{2+} content. For instance, broad ν_3 signals observed at 1092 and 1034 cm^{-1} in Ca100 shift to 1076 and 1028 cm^{-1} in Sr100, respectively. Analogously, from Ca100 to Sr100, ν_1 moves from 962 to 947 cm^{-1} and the two signals attributed to ν_4 (sharp) shift from 602 and 565 cm^{-1} to 594 cm^{-1} and 561 cm^{-1}, respectively. Finally, the very weak ν_2 signal is found at 472 cm^{-1} for Ca100 and at 463 cm^{-1} in Sr100 nanopowders, respectively. Conversely, the signals related to HA-lattice OH groups

are observed at 3572 cm^{-1} (stretching) and 633 cm^{-1} (bending) in all samples, although they gradually vanish at higher Sr content.

Further and more accurate information can be obtained by observing the signals in the 500-700 cm^{-1} range, including the two peaks due to PO_4^{3-} v_4 band and the OH bending vibration at 633 cm^{-1}. In particular, the most intense peak around 565 cm^{-1} gradually broadens and then for Sr100 it shrinks revealing two shoulders at 573 and 538 cm^{-1}, this latter assigned to HPO_4^{2-} groups [27]. To quantify these changes, according to the literature [28], the profile fitting analysis of signals in the 500-700 cm^{-1} range was performed with six components accounting for hydroxyl groups, surface and internal phosphate groups (Tab. 2). Deconvolution and peaks integration were performed on spectra whose intensity was normalized by the corresponding v_3 signal at ~1092 cm^{-1}.

Sample	surface HPO$_x$		internal PO$_4^{3-}$ (1)		internal PO$_4^{3-}$ (2)		internal PO$_4^{3-}$ (3)		surface PO$_x$		δ OH$^-$	
	Pos., ±2 cm^{-1}	Rel. Area, %	Pos., ±2 cm^{-1}	Rel. Area, %	Pos., ±2 cm^{-1}	Rel. Area, %	Pos., ±2 cm^{-1}	Rel. Area, %	Pos., ±2 cm^{-1}	Rel. Area, %	Pos., ±2 cm^{-1}	Rel. Area, %
Ca100	538	0.4	565	34.6	574	18.1	602	16.7	606	3.0	633	27.4
Sr5	537	8.2	564	29.1	574	18.1	603	22.6	616	3.7	634	18.4
Sr10	540	6.4	563	19.8	571	26.0	602	22.6	614	8.3	635	17.0
Sr25	538	4.2	563	34.4	573	11.4	600	30.9	610	5.6	633	13.6
Sr50	538	8.3	561	25.2	571	21.5	598	22.7	604	12.4	633	9.9
Sr75	538	17.0	559	25.5	572	12.1	595	25.5	603	13.8	633	6.0
Sr100	538	9.1	561	35.0	573	9.5	593	26.6	599	14.3	633	5.4

Tab. 2: FTIR signals deconvolution in the range 500-700 cm^{-1} (v_4 domain) using components proposed in [28].

Representative TEM nanopowder micrographs are reported in Fig. 2 showing rod shape geometry with different size and aggregation state. The smallest structures (major axis around 45 ± 14 nm) were observed in Ca100 sample and the nanopowders appeared well separated. In Sr-containing samples enhanced aggregation is observed with an increase in particle size if compared to Ca100 sample. In particular, Sr-containing powders show a more elongated morphology and the length of major axis increases with Sr amount up to 124 ± 42 nm for Sr100 (Tab. 03).
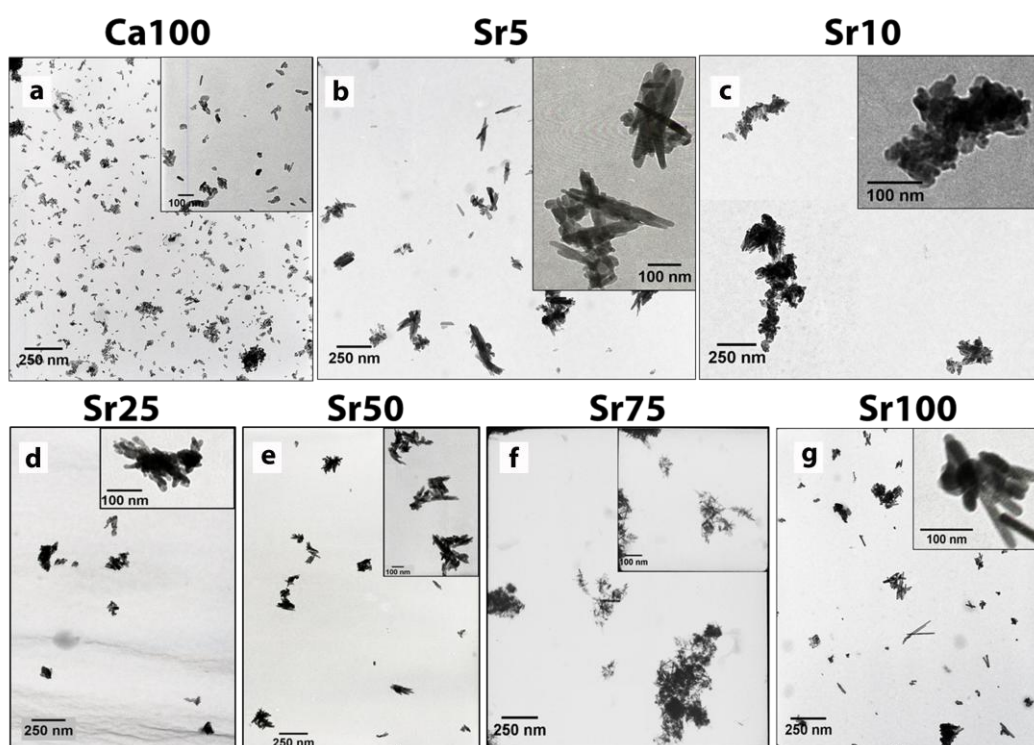
Fig 2: Representative TEM images of HA nanopowders doped with increasing concentrations of Sr. In detail: Ca100 (a), Sr5 (b), Sr10 (c), Sr25 (d), Sr50 (e), Sr75 (f) and Sr100 (g), respectively. The scale bar shown represents 250 nm in all panels and 100 nm in all inserts.

The N_2 adsorption-desorption isotherms collected on all samples (Fig. S-1 in the SM) are characterized by a IIb-type curve with an H3 hysteresis loop and no plateau at high pressures. These features are representative of meso- and macro-porous materials constituted by aggregated non-isomorphic particles. The corresponding pore size distribution confirms the presence of a broad range of pores larger than 180-200 Å. By increasing the Sr amount, specific surface area and total pore volume show a fluctuating trend scattered around 50 m^2/g and 0.300 cm^3/g, respectively. It is interesting to observe that the measured SSA well scales with the average particles dimension (D) determined by TEM analysis through the well know relationship

$$D = \psi / (\rho \, SSA) \qquad\qquad (1)$$

where ρ is the density (equal to 3.08 g/cm^3 for CaHA, 3.84 g/cm^3 for SrHA) and ψ is a shape factor equal to ~ 6; assuming SSA = 50 m^2/g, one can obtain D = 31 nm for CaHA and 39 nm for SrHA. Such values well compare with particles size shown in Tab. 3 considering the wide

scatter observed especially for larger Sr content. This also confirms that the synthesized nanoparticles are dense and that the considered porosity is substantially related to voids among particles.
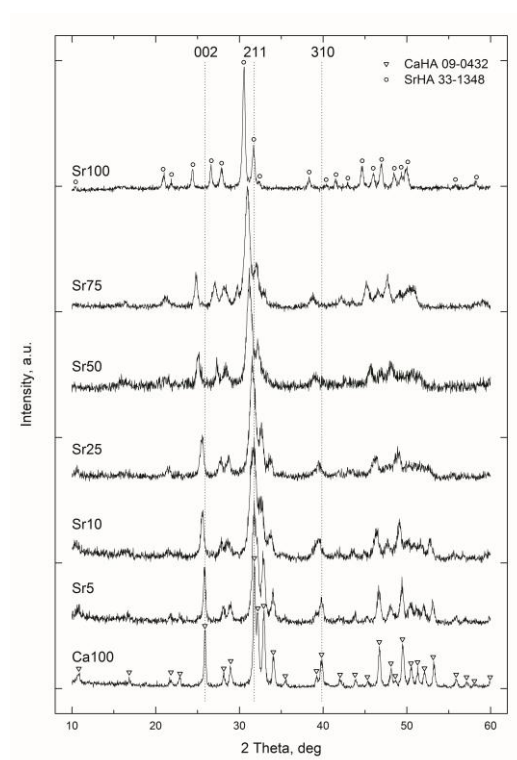

Fig 3: XRD patterns of the synthesized Sr-Hydroxyapatite nanopowders. Vertical dotted lines highlight Ca100 main reflection (211), and planes (002) and (310), respectively normal and parallel to the *c* axis.

XRD patterns collected on synthesized nanopowders are shown in Fig 3. The two endpoints of the composition series (i.e., Ca100 and Sr100) display quite sharp peaks that are perfectly matched by pure calcium-hydroxyapatite (JCPDS no: 09-0432) and pure strontium-hydroxyapatite (JCPDS no: 33-1348) phases. Conversely, the remaining compositions show reflections at intermediate positions, according to the increasing amount of Ca^{2+} substituted by Sr^{2+}. At the same time, the peak width increases and the signal-to-noise ratio decreases along the series, as expected for a nanocrystalline material. The average crystallite sizes calculated using the Warren-Averbach method confirm this observation; values are included in the 20-30 nm interval for the intermediate samples, reaching 52 nm (Ca100) and 41 nm (Sr100) for the two limit structures (Tab. 3).

	(002)	(310)	Cell parameters and crystallite size (XS)				TEM
Sample	Position, ±0.03 deg	Position, ±0.03 deg	a, Å	c, Å	c/a, ± 0.001	XS, ± 1 nm	Rod-shape length, nm
Ca100	25.87	39.85	9.423 ± 0.001	6.881 ± 0.001	0.730	52	45 ± 14
Sr5	25.81	39.80	9.435 ± 0.003	6.899 ± 0.002	0.731	31	72 ± 15
Sr10	25.63	39.64	9.461 ± 0.004	6.921 ± 0.003	0.732	19	83 ± 24
Sr25	25.57	39.45	9.507 ± 0.005	6.974 ± 0.004	0.734	30	98 ± 17
Sr50	25.18	39.17	9.609 ± 0.008	7.087 ± 0.007	0.738	25	113 ± 32
Sr75	24.82	38.76	9.668 ± 0.005	7.166 ± 0.004	0.741	19	121 ± 22
Sr100	24.40	38.32	9.776 ± 0.002	7.289 ± 0.002	0.746	41	124 ± 42

Tab. 3: XRD (002) and (310) peaks position for the synthesized nanopowders; unit cell parameters and crystallite sizes obtained by XRD pattern refinement and particle length from TEM observations are also shown.

^{1}H MAS NMR signals (Fig 4a) are quite resolved, with a sharp peak at 0.22 ppm (Ca100) assigned to OH groups in HA crystal lattice [29], which presents a high-field shift and an increase in asymmetry with increasing Sr^{2+} content. Furthermore, the proton spectra show the broad water resonance around 5-7 ppm and up to three additional small sharp peaks, randomly observable at 1-3 ppm, probably due to surface adsorbed water [30]. The lineshape analyses of OH peaks was performed in the range -2.0-1.5 ppm by introducing a central main component and two minor side components and the results are reported in Tab. S-1 in the SM.
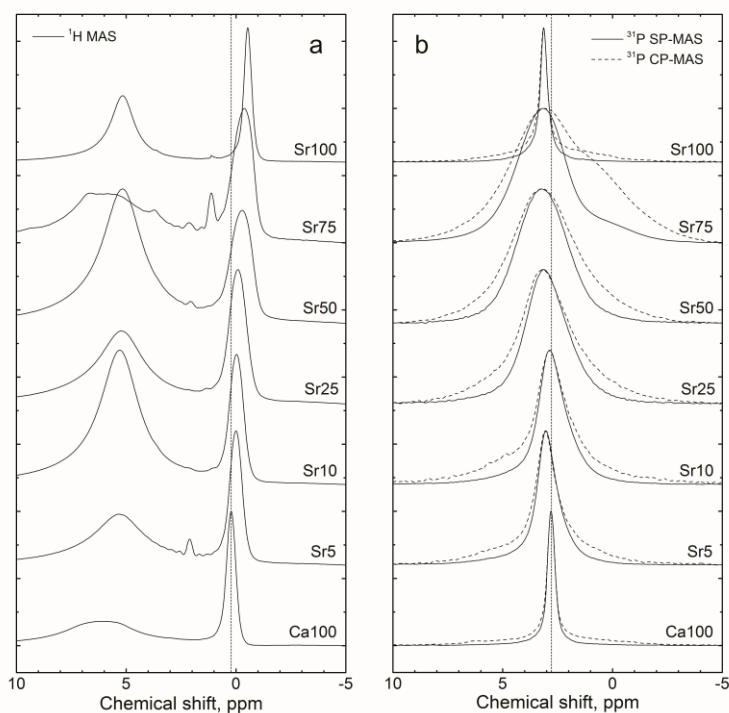
Fig 4: Solid state NMR spectra of the synthesized Sr-Hydroxyapatite nanopowder. In detail: a) ^{1}H MAS; b) ^{31}P SP-MAS (straight line) and ^{31}P CP-MAS (dashed line). Vertical dotted lines show the Ca100 main signals.

^{31}P SP-MAS NMR experiments show a behaviour consistent with previous evidences achieved by FT-IR and XRD analysis: the spectra (Fig. 4b, solid line), contain a resolved peak at 2.80 ppm (Ca100), which progressively broadens and shifts to lower fields for increasing Sr^{2+} amount, before narrowing again for Sr100 sample. This tendency is emphasized in the ^{31}P CP-MAS NMR spectra (Fig. 4b, dashed line), where the additional polarization from protons allows to identify a main sharp signal, associable with internal PO_4^{3-} groups, and two broad overlapped resonances leading to shoulders at 3.13 and 2.51 ppm (Ca100) related with $-PO_x$ and $-HPO_x$ surface groups [31]. Consequently, ^{31}P SP spectra deconvolution was performed employing these components (Tab. S-2 in the SM). The results point out the low-field shift and broadening of the internal PO_4^{3-} component up to 50% of strontium load. Further increase of Sr^{2+} content leads to linewidth reduction and moves back the signal towards high fields. Unfortunately, no clear trends can be observed for the minor components.

The hydrodynamic diameter (Tab. 4) determined on nanoparticle suspensions by DLS at different times is always about twice the size determined by TEM, clearly increasing from Ca100S to Sr100S. No evident trend was recorded for ζ potential as a function of Sr content, the values being always quite scattered and ranging between -5.3 and -8.4.

Sample	Hydrodynamic diameter (nm)
Ca100S	98 ± 30
Sr5S	126 ± 26
Sr10S	157 ± 31
Sr25S	207 ± 64
Sr50S	228 ± 77
Sr75S	224 ± 54
Sr100S	228 ± 91

Tab. 4: Hydrodynamic diameter measured by DLS technique on nanopowder suspensions.

The FTIR spectra recorded on the suspensions were significantly different from those corresponding to the mere physical mixtures (Fig. S-2 in the SM). The main differences concern the phosphate group peaks, the ν_3 signals intensity decreasing with Sr load; a new peak is also evident at about 1074 cm^{-1} in the suspensions spectra. In addition, two new peaks at 941 and 858 cm^{-1} appear in Sr25S, Sr50S, Sr75S and Sr100S spectra.

3.2 Cell viability, apoptosis and morphology

Cell viability determined by the MTT test is shown in Fig. 5 for SAOS-2 cells incubated with increasing suspension concentrations at 1, 3 and 7 days. The data are shown considering 100% viability when no nanoparticles are present. The viability is generally positively influenced by the presence of larger suspension load at longer incubation times. After 24 h, no significant differences ($p>0.05$) are observed between untreated or treated cells regardless the type of the suspension (Fig. 5a). After 3 days of culture, viability is 30% higher in samples treated with Sr50S (625 µg/mL), Sr75S (625 µg/mL) and Sr100S (62.5 µg/mL) (Fig. 5b). After 1 week, an increment from 25% up to 37% is observed in sample treated with Sr25S (625 µg/mL), Sr50S (625 µg/mL), Sr75S (625 µg/mL) and Sr100S (62.5 µg/mL) (Fig. 5c).
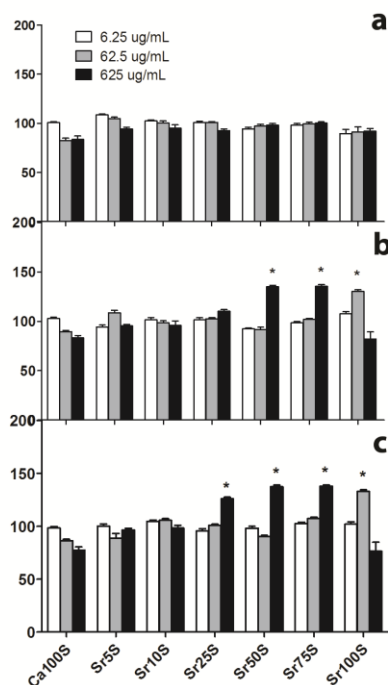

Fig 5: Dose- and time-dependent effect of the different types of nanoparticles suspensions on SAOS-2 cell viability. SAOS-2 cells were treated with three increasing concentrations of each type of nanoparticles dispersed in 0.5% BSA at three different times: 1 (panel a), 3

(panel b) and 7 (panel c) days, respectively. Results of MTT test are expressed as percentage related to untreated cells set as 100%. Level of significance: * $p < 0.05$

Cell proliferation increases in samples treated with larger Sr amount (Sr25S, Sr50S, Sr75S and Sr100S). Similar results were obtained by using the Resazurin-based test.

In order to evaluate cell apoptosis caused by nanoparticle suspensions treatment, PSVue® 480 and Hoechst staining were performed at 24 h (Fig. S-3 in the SM). After 24h, as expected, SAOS-2 cells exhibit a clear green fluorescence after hydrogen peroxide treatment, showing high level of apoptosis. Green fluorescence in H_2O_2 treated sample is very intense to cover the blue fluorescence of Hoechst. Conversely, fluorescent analysis of untreated and treated cells are negative after staining with PSVue480™ reagent, indicating that all treatments do not induce cell apoptosis. Similar data were obtained after 7 days treatment.

SEM images were recorded on control cells and cells treated with 625 µg/mL. Figure 6 shows representative images of cells untreated and treated with Ca100S, Sr50S and Sr100S at 1 and 7 days of culture. As expected, in all samples, the typical SAOS-2 cells morphology is shown and no differences were observed between treated and untreated cells.
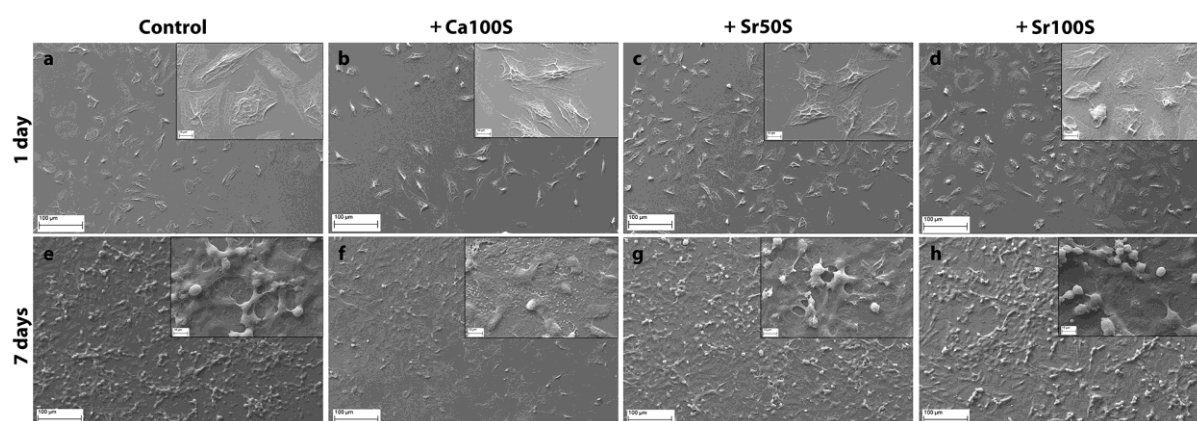

Fig 6: Representative SEM images of untreated and treated SAOS-2 cells with nanoparticles suspensions. Images were taken after 1 (a, b, c and d) and 7 (e, f, g and h) days of treatment in the following conditions: untreated (a and e) and treated cells with 1250 µg/mL of Ca100S (b and f), Sr50S (c and g) and Sr100S (d and h), respectively. The scale bar shown represents 100 mm in all panels and 10 mm in all inserts.

4. DISCUSSION

The structural characterization of the nanopowders carried out by FTIR, XRD and NMR clearly points out valuable differences accounted for by the replacement of calcium with strontium.

$Ca^{2+} \rightarrow Sr^{2+}$ substitution leads to a progressive modification of the particle shape along a preferential direction, i.e. parallel to *c-axis*, as observed in the TEM micrographs (Fig. 2). At the same time, the crystalline cell is coherently subjected to an anisotropic linear growth that involves *c* parameter more than *a* parameter (Tab.3). The effect is further underlined observing the growing trend of *c/a* ratio, where linear regression supplies very good fittings of the experimental data. If such values are plotted as a function of the particle length distribution obtained by TEM (Fig. 7), a logarithmic-like dependence is found: for limited amount of Sr the crystal elongation highly influences the final particle size, the effect being more limited for larger Sr content.
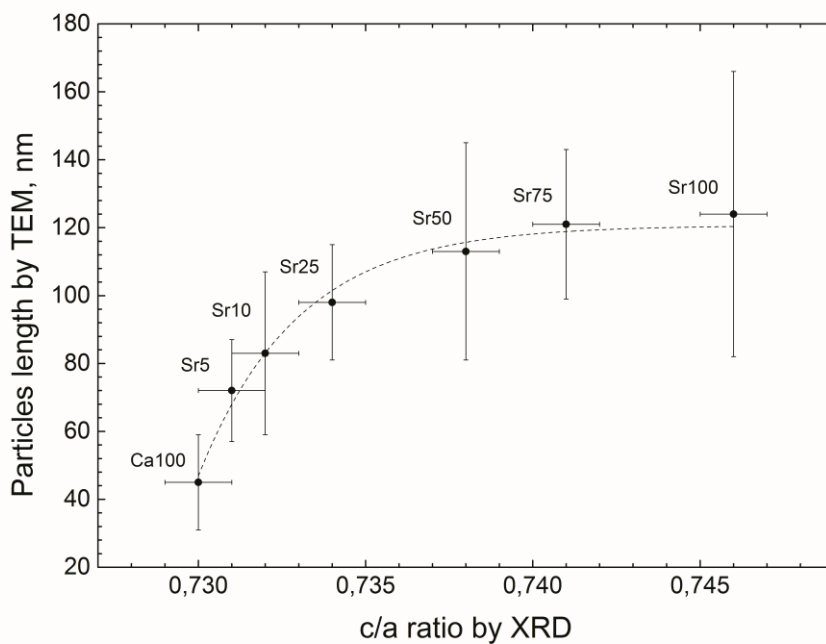

Fig 7: Correlation between the nanoparticle length (by TEM), and the cell parameters *c/a* ratio (by XRD pattern refinement) increasing the Sr content in the synthesized HA nanopowders.

Strontium causes drastic modifications in the local chemical environment of the apatitic functional groups, PO_4 and crystalline OH, resulting in clearly observable changes in FT-IR and NMR spectra. The OH bending signal (δ OH: 633 cm^{-1}) intensity reduction with

Sr load is clearly pointed out by the deconvolution of FT-IR bands in the range 500-700 cm^{-1} (Tab. 2). The values of δ OH integrated area well relate with the *c/a* ratio (Fig 8) showing an exponential decrease with increasing cell deformation. It has to be recalled that hydroxyl groups are located along the *c-axis*, within interstices shaped by three M(2)-type cations forming planar triangles, perpendicular to the O-H bonds. The contemporary presence of both Sr^{2+} and Ca^{2+} ions in the M(2) positions generates a strong perturbation in the lattice in terms of ionic radius and electronegativity. Moreover, the anisotropic elongation of the crystalline cells along the *c-axis* entails a decrease in spatial density of O-H bonds, i.e. more limited bonds per unit volume. These conditions probably affect the hydroxyl vibrational mode, causing the reduction of the corresponding FT-IR absorption signal. The modified structural environment affects also the crystalline OH signals in ^{1}H MAS NMR spectra, leading to a shift towards higher fields with increasing Sr amount. (Tab. S-1 in the SM)
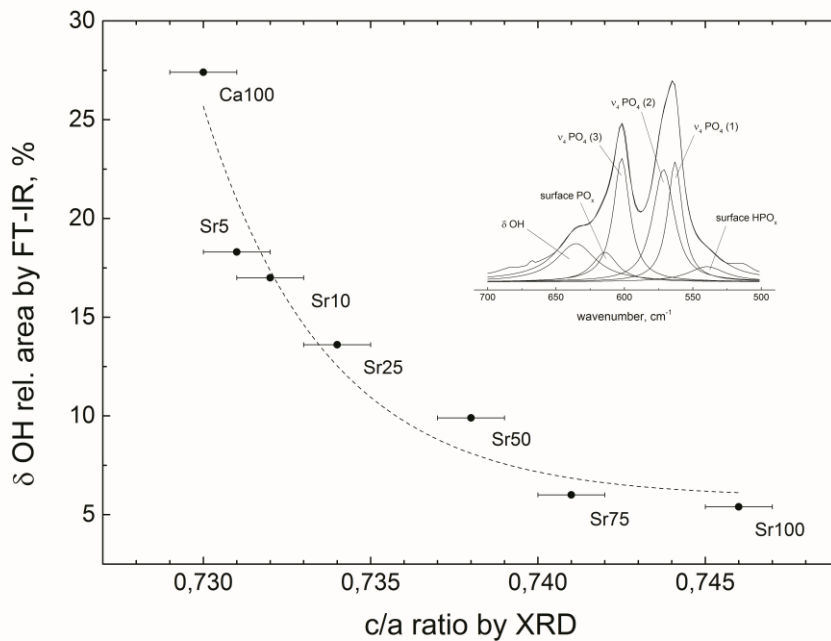

Fig 8: Correlation between relative area of δ$_{OH}$ signal (obtained by deconvolution of ν$_4$ FT-IR band), and cell parameters *c/a* ratio (obtained by XRD pattern refinement) increasing the Sr content in the synthesized HA nanopowders. In the top right corner, representative example of ν$_4$ FT-IR deconvolution with six components (Sr10 composition).

The deconvoluted FT-IR ν$_4$-PO$_4$ components (1) and (3) (internal PO$_4$: 565 and 602 cm^{-1}) shift to lower wavenumbers following a linear trend with Sr content. Such vibrational frequency decrease has been already accounted for in previous works [32] by considering the

energy loss of some P-O bonds, upon the increase of the reciprocal distance between the PO_4 groups, as a consequence of the lattice expansion. For the same reason, the ^{31}P SP-MAS signals of internal PO_4 (Tab. S-2 in the SM) present a low-field shift.

One last comment regarding the Sr influence can be drawn by observing the line broadening (as FWHM) of the deconvoluted main components of ^{31}P SP-MAS (internal PO_4) and ^{1}H MAS (crystalline OH) signals, reported as a function of Sr amount in Fig. 9. Since NMR is extremely sensitive to the different chemical environments surrounding a specific element, it is quite clear that the lower presence of substitutional ion (Sr^{2+} or Ca^{2+}) is perceived by the remaining HA lattice (Ca^{2+} or Sr^{2+}) as a point defect. The maximum disorder (i.e., the maximum line broadening) is reached for the Sr50 composition, where Sr and Ca atoms are in equal number and they both constitute defects. This short-range variability seems to prevent also crystallization, leading to broader and noisier XRD spectra and smaller crystallite size than in Ca100 and Sr100 limit structures.
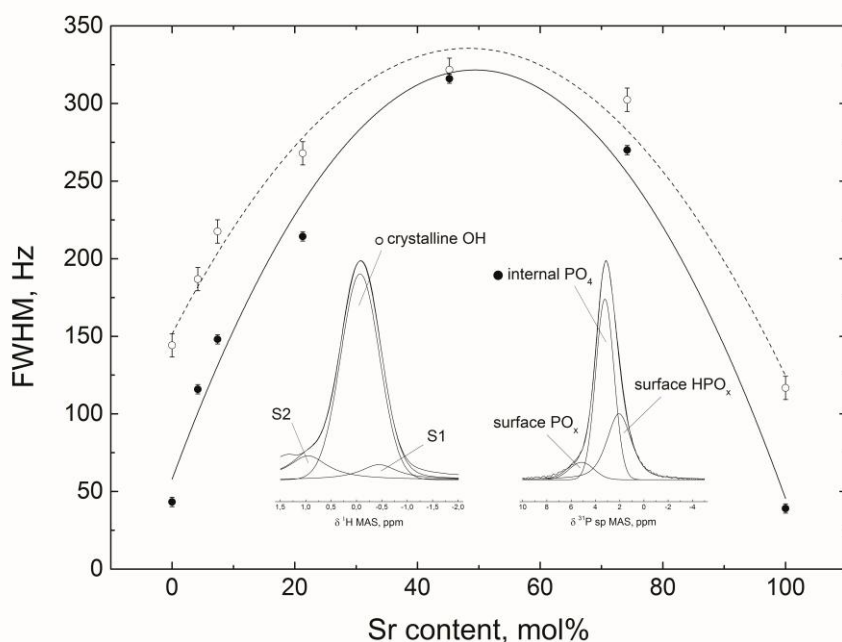

Fig 9: Line broadening (FWHM) of the deconvoluted main components of ^{1}H MAS spectra (crystalline OH, empty circles and dotted line) and of ^{31}P SP-MAS spectra (internal PO_4, full circles and straight line) as a function of Sr content in the synthesized HA nanopowders. On the bottom, representative example of ^{1}H SP-MAS (left) and ^{31}P SP-MAS (right) signal deconvolution with three components (Sr25 composition).

However, XRD and NMR results do not provide any evidence of the formation of distinct mono-cation phases. Both XRD and NMR spectra show a gradual evolution between the two limit compositions, Ca100 and Sr100, thus proving the homogeneity of the synthesized nanopowders and the complete solubility of strontium in HA lattice.

The nanopowder surface features, such as SSA and total pore volume, and the components related to surface HPO_x and PO_x groups in FT-IR and NMR spectra, seem to depend to a lower extent on Sr content, showing scattered values and apparently no regular trends. Wang et al. [33] recently stated that natural and synthetic apatites are coated by an amorphous hydrated layer. The surface phosphate groups randomly interact with the adsorbed water molecules, whose amount depends on the storing conditions. Such aleatory contribution, which can be removed only by drying, precludes a more detailed analysis of the Sr effect on the nanopowder surface properties.

In order to perform *in vitro* biocompatibility studies, nanoparticles were dispersed with BSA fluid. Albumin is one of the most representative proteins in human blood and one of its functions is to bind hydrophobic molecules and carry them through the body tissues. To promote the bond between nanopowders and the protein, a physical treatment consisting of heating and sonication was performed here. The thermal treatment promotes a partial denaturation of the protein that, losing its natural folding, exposes more functional groups to bind hydroxyapatite crystals [34]; conversely, sonication destroys nanopowders aggregates thus allowing a more efficient surface bond with the protein molecules. This interaction was investigated using IR technique revealing modifications of the peaks related to phosphate groups (Fig. S-2 in the SM) suggesting a potential role in the interaction with BSA. Other differences were observed in IR spectra although further investigations are necessary for a deeper understanding of the interaction.

The $Ca^{2+} \rightarrow Sr^{2+}$ substitution influences the hydrodynamic diameter, which is always twice the particles size determined by TEM analysis. A certain contribution of BSA on the hydrodynamic diameter has to be considered, which, however, does not account for the formation of any aggregate. The evaluation of suspensions stability by measuring ζ potential revealed the presence of negative charges on the nanoparticles surface with no valuable differences among the different suspensions. ζ potential was also separately measured by DLS for nanopowders and BSA in water and values around zero were obtained. Therefore, the negative values determined for the suspensions suggest BSA rearrangement upon the interaction with nanoparticles surface, which results in exposing negative charges to the solvent and in the suspension stabilization [35].

Nanoparticle suspensions exhibit high biocompatibility as confirmed by viability results and cell morphology evolution. Nanoparticles composition and dose and culture time influence cells proliferation. In general, the proliferation increases in samples treated with nanoparticles containing larger Sr content and after longer incubation times. These results suggest a specific correlation between Sr concentration in the medium and cell viability: for samples treated with Sr100S, the cell proliferation increase was observed at concentration of 62.5 µg/mL whereas similar increments were detected in samples treated with Sr25S, Sr50S or Sr75S at concentration 10 time larger (625 µg/mL). Conversely, samples treated for 3 or 7 days with Sr100S at 625 µg/mL show a non-statistically significant cell viability decrease. Since no apoptosis was observed in these samples, the effect is likely to be related to the cell proliferation rate and not to the cell killing, or to an excessive Sr treatment that could activate other metabolisms leading to a cell proliferation decrease. Further studies are needed to clarify this point. Scaffolds made by HA containing 7% Sr have been reported to affect osteoblast proliferation [17, 20] but there are no data about the real amount of Sr whereby cells were treated. Instead, Sr ranelate concentration that has a positive effect on osteoblast proliferation is comparable with Sr concentration treatments in our study. Using ICP results, Sr concentration in the culture media is around 1 mM, which matches previous results shown to be effective in promoting osteoblast viability and proliferation [13, 36, 37].

5. CONCLUSIONS

In the present work, strontium-substituted hydroxyapatite nanopowders were systematically synthesized by aqueous precipitation in the range of 0-100 mol% Sr. One single crystalline phase is always obtained, Ca and Sr occupying the same lattice position in the HA structure. The replacement of Ca^{2+} by Sr^{2+} ions with different ionic radius and electronegativity leads to the nanopowders modification at different structural levels. Pure Sr-HA and Ca-HA nanopowders are characterized by larger crystallite size ($50 - 60$ nm) with respect to intermediate compositions (20-30 nm). As for powder morphology, a progressive and strongly anisotropic growth along c direction is induced by Sr. Correspondingly, crystalline unit cells are subjected to an expansion which is larger along c than along a; this causes functional group rearrangements, responsible for weaker P-O bonds and, above all, for evident OH spatial density changes and their local environment.

The synthesized powders can be easily used for the preparation of water suspensions with the addition of Bovine Serum Albumin. Such biological protein interacts positively with the nanopowders surface, stabilizing the suspension and avoiding the formation of any aggregate.

The produced suspensions are biocompatible with no apoptotic effect on osteoblast cells. Suspensions prepared with nanopowders containing larger Sr amount clearly promote osteoblast viability and proliferation.

The obtained results point out that strontium-substituted hydroxyapatite nanoparticles could be potentially employed to delivery Sr to bone tissue and promote its regeneration, as component of bone substitute synthetic materials, additive for pharmaceutical preparation or food supplementary for systemic distribution.

REFERENCES

[1]   Dorozhkin, S. V. Self-Setting Calcium Orthophosphate Formulations: Cements, Concretes, Pastes and Putties. *Int. J. Mater. Chem.* **2012**, *1*, 1–48.

[2]   Champion, E. Sintering of calcium phosphate bioceramics. *Acta Biomater.* **2013**, *9*, 5855–5875.

[3]   Frasnelli, M.; Sglavo, V.M. Effect of Mg(2+) doping on beta-alpha phase transition in tricalcium phosphate (TCP) bioceramics. *Acta Biomater.* **2016**, *33*, 283–9.

[4]   Narayanan, R.; Seshadri, S.K.; Kwon, T.Y.; Kim, K.H. Calcium phosphate-based coatings on titanium and its alloys. *J. Biomed. Mater. Res. Part B Appl. Biomater.* **2008**, *85B*, 279–299.

[5]   Gòmez-Morales, J.; Iafisco, M.; Delgado-Lòpez, J.M.; Sarda, S.; Drouet, C. Progress on the preparation of nanocrystalline apatites and surface characterization: Overview of fundamental and applied aspects. *Prog. Cryst. Growth Charact. Mater.* **2013**, *59*, 1–46.

[6]   McElderry, J.-D.P.; Zhu, P.; Mroue, K.H.; Xu, J.; Pavan, B.; Fang, M.; Zhao, G.; McNerny, E.; Kohn, D.H.; Franceschi, R.T.; Holl, M.M.B.; Tecklenburg, M.M.J.; Ramamoorthy, A.; Morris, M.D. Crystallinity and compositional changes in carbonated apatites: Evidence from (31)P solid-state NMR, Raman, and AFM analysis. *J. Solid State*

Chem. **2013**, *206*, 192–198.

[7]   Laurencin, D.; Almora-Barrios, N.; de Leeuw, N.H.; Gervais, C.; Bonhomme, C.; Mauri, F.; Chrzanowski, W.; Knowles, J.C.; Newport, R.J.; Wong, A.; Gan, Z.; Smith, M.E. Magnesium incorporation into hydroxyapatite. *Biomaterials* **2011**, *32*, 1826–37.

[8]   Lijuan, X.; Liuyun, J.; Chengdong, X.; Lixin, J. Effect of different synthesis conditions on the microstructure, crystallinity and solubility of Mg-substituted hydroxyapatite nanopowder. *Adv. Powder Technol.* **2014**, *25*, 1142–1146.

[9]   Cox, S.C.; Jamshidi, P.; Grover, L.M.; Mallick, K.K. Preparation and characterisation of nanophase Sr, Mg, and Zn substituted hydroxyapatite by aqueous precipitation. *Mater. Sci. Eng. C. Mater. Biol. Appl.* **2014**, *35*, 106–14.

[10]   Abert, J.; Bergmann, C.; Fischer, H. Wet chemical synthesis of strontium-substituted hydroxyapatite and its influence on the mechanical and biological properties. *Ceram. Int.* **2014**, *40*, 9195–9203.

[11]   Kinney, E.; McCollum, E. A study of the rate of deposition and paths of absorption of strontium in the rat. *J. Pharmacol.* **1922**, *22*, 165–176.

[12]   Querido, W.; Rossi, A.L.; Farina, M. The effects of strontium on bone mineral: A review on current knowledge and microanalytical approaches. *Micron* **2015**, *80*, 122–134.

[13]   Barbara, A.; Delannoy, P.; Denis, B.; Marie, P. Normal matrix mineralization induced by strontium ranelate in MC3T3-E1 osteogenic cells. *Metabolism* **2004**, *53*, 532–537.

[14]   Grosso, A.; Douglas, I.; Hingorani, A.; MacAllister, R.; Smeeth, L. Post-marketing assessment of the safety of strontium ranelate; a novel case-only approach to the early detection of adverse drug reactions. *Br. J. Clin. Pharmacol.* **2008**, *66*, 689–94.

[15]   Bigi, A.; Boanini, E.; Capuccini, C.; Gazzano, M. Strontium-substituted hydroxyapatite nanocrystals. *Inorganica Chim. Acta* **2007**, *360*, 1009–1016.

[16]   Li, Y.; Li, Q.; Zhu, S.; Luo, E.; Li, J.; Feng, G.; Liao, Y.; Hu, J. The effect of strontium-substituted hydroxyapatite coating on implant fixation in ovariectomized rats. *Biomaterials* **2010**, *31*, 9006–9014.

[17]   Capuccini, C.; Torricelli, P.; Sima, F.; Boanini, E.; Ristoscu, C.; Bracci, B.; Socol, G.; Fini, M.; Mihailescu, I.N.; Bigi, A. Strontium-substituted hydroxyapatite coatings synthesized by pulsed-laser deposition: In vitro osteoblast and osteoclast response. *Acta Biomater.* **2008**, *4*, 1885–1893.

[18]   Raucci, M.G.; Giugliano, D.; Alvarez-Perez, M. a.; Ambrosio, L. Effects on growth and osteogenic differentiation of mesenchymal stem cells by the strontium-added sol–gel hydroxyapatite gel materials. *J. Mater. Sci. Mater. Med.* **2015**, *26*, 90.

[19]   Kitayama, S.; Wong, L.O.; Ma, L.; Hao, J.; Kasugai, S.; Lang, N.P.; Mattheos, N.

Regeneration of rabbit calvarial defects using biphasic calcium phosphate and a strontium hydroxyapatite-containing collagen membrane. *Clin. Oral Implants Res.* **2015**, *00*, 1–9.

[20]   Capuccini, C.; Torricelli, P.; Boanini, E.; Gazzano, M.; Giardino, R.; Bigi, A. Interaction of Sr-doped hydroxyapatite nanocrystals with osteoclast and osteoblast-like cells. *J. Biomed. Mater. Res. A* **2009**, *89*, 594–600.

[21]   Holthoff, H.; Egelhaaf, S.U.; Borkovec, M.; Schurtenberger, P.; Sticher, H. Coagulation Rate Measurements of Colloidal Particles by Simultaneous Static and Dynamic Light Scattering. *Langmuir* **1996**, *12*, 5541–5549.

[22]   Lauten, R.A.; Kjøniksen, A.-L.; Nyström, B. Colloid Polymer Interactions and Aggregation in Aqueous Mixtures of Polystyrene Latex, Sodium Dodecyl Sulfate, and a Hydrophobically Modified Polymer: A Dynamic Light Scattering Study. *Langmuir* **2001**, *17*, 924–930.

[23]   Risi, G.; Bloise, N.; Merli, D.; Icaro-Cornaglia, A.; Profumo, A.; Fagnoni, M.; Quartarone, E.; Imbriani, M.; Visai, L. In vitro study of multiwall carbon nanotubes (MWCNTs) with adsorbed mitoxantrone (MTO) as a drug delivery system to treat breast cancer. *RSC Adv.* **2014**, *4*, 18683.

[24]   Van Engeland, M.; Nieland, L.J.W.; Ramaekers, F.C.S.; Schutte, B.; Reutelingsperger, C.P.M. A review on an apoptosis detection system based on phosphatidyserine exposure. *Citometry* **1998**, *31*, 1–9.

[25]   Saino, E.; Ph, D.; Maliardi, V.; Sc, M.; Quartarone, E.; Fassina, L.; Benedetti, L.; Gabriella, M.; Angelis, C. De; Mustarelli, P.; Facchini, A.; Visai, L. In Vitro Enhancement of SAOS-2 Cell Calcified Matrix Deposition onto Radio Frequency Magnetron Sputtered Bioglass-Coated Titanium Scaffolds. *Tissue Eng. Part A* **2010**, *16*, 995–1008.

[26]   Koutsopoulos, S. Synthesis and characterization of hydroxyapatite crystals: a review study on the analytical methods. *J. Biomed. Mater. Res.* **2002**, *62*, 600–12.

[27]   Kaflak, A.; Kolodziejski, W. Complementary information on water and hydroxyl groups in nanocrystalline carbonated hydroxyapatites from TGA, NMR and IR measurements. *J. Mol. Struct.* **2011**, *990*, 263–270.

[28]   Šupová, M. Substituted hydroxyapatites for biomedical applications: A review. *Ceram. Int.* **2015**, *41*, 9203–9231.

[29]   Kolmas, J.; Kolodziejski, W. Inverse 31P→1H NMR cross-polarization in hydrated nanocrystalline calcium hydroxyapatite. *Chem. Phys. Lett.* **2012**, *554*, 128–132.

[30]   Munarin, F.; Petrini, P.; Gentilini, R.; Pillai, R.S.; Dirè, S.; Tanzi, M.C.; Sglavo, V.M. Micro- and nano-hydroxyapatite as active reinforcement for soft biocomposites. *Int J Biol Macromol* **2015**, *Jun*, 199–209.

[31]   Kolmas, J.; Ślósarczyk, A.; Wojtowicz, A.; Kolodziejski, W. Estimation of the specific surface area of apatites in human mineralized tissues using 31P MAS NMR. *Solid State Nucl. Magn. Reson.* **2007**, *32*, 53–58.

[32]   Fowler, B.O. Infrared studies of apatites. II. Preparation of normal and isotopically substituted calcium, strontium, and barium hydroxyapatites and spectra-structure-composition correlations. *Inorg. Chem.* **1974**, *13*, 207–214.

[33]   Wang, Y.; Von Euw, S.; Fernandes, F.M.; Cassaignon, S.; Selmane, M.; Laurent, G.; Pehau-Arnaudet, G.; Coelho, C.; Bonhomme-Coury, L.; Giraud-Guille, M.-M.; Babonneau, F.; Azaïs, T.; Nassif, N. Water-mediated structuring of bone apatite. *Nat. Mater.* **2013**, *12*, 1144–1153.

[34]   Picò, G. Thermodynamic aspects of thermal stability of human serum albumin. *Biochem. Mol. Biol. Int.* **1995**, *36*, 1017–1023.

[35]   Salis, A.; Bostr, M.; Medda, L.; Cugia, F.; Barse, B.; Parsons, D.F.; Ninham, B.W.; Monduzzi, M. Measurements and Theoretical Interpretation of Points of Zero Charge / Potential of BSA Protein. *Langmuir* **2011**, *27*, 11597–11604.

[36]   Takahashi, N.; Sasaki, T.; Tsouderos, Y.; Suda, T. S 12911-2 Inhibits Osteoclastic Bone Resorption In Vitro. *J. Bone Miner. Res.* **2003**, *18*, 1082–1087.

[37]   Lariboisiere, H.; Cultures, C. The Divalent Strontium Salt S12911 Enhances Bone Cell. *Bone* **1996**, *18*, 517–523.

Supplementary Data
Click here to download Supplementary Data: Supplementary Material.docx